TECHNICAL ARTICLE

Evolution in the structure of akaganeite and hematite during hydrothermal growth: an *in situ* synchrotron X-ray diffraction analysis

Kristina M. Peterson,[1,a)] Peter J. Heaney,[2] and Jeffrey E. Post[3]

[1]*Lyell Centre, Heriot Watt University, Edinburgh, UK*
[2]*Department of Geosciences, Pennsylvania State University, University Park, Pennsylvania 16802*
[3]*Department of Mineral Sciences, Smithsonian Institution, Washington, District of Columbia 20560-0119*

Synchrotron X-ray diffraction was used to monitor the hydrothermal precipitation of akaganeite (β-FeOOH) and its transformation to hematite (Fe_2O_3) *in situ*. Akaganeite was the first phase to form and hematite was the final phase in our experiments with temperatures between 150 and 200 °C. Akaganeite was the only phase that formed at 100 °C. Rietveld analyses revealed that the akaganeite unit-cell volume contracted until the onset of dissolution, and subsequently expanded. This reversal at the onset of dissolution was associated with a substantial and rapid increase in occupancy of the Cl site, perhaps by OH^- or Fe^{3+}. Rietveld analyses supported the incipient formation of an OH-rich, Fe-deficient hematite phase in experiments between 150 and 200 °C. The inferred H concentrations of the first crystals were consistent with "hydrohematite." With continued crystal growth, the Fe occupancies increased. Contraction in both *a*- and *c*-axes signaled the loss of hydroxyl groups and formation of a nearly stoichiometric hematite. © 2018 International Centre for Diffraction Data. [doi:10.1017/S0885715618000623]

Key words: TR-XRD, akaganeite, hematite, hydrohematite, hydrothermal, Rietveld refinements

I. INTRODUCTION

Iron oxides and oxyhydroxides are abundant in terrestrial environments, where they play a central role in iron cycling, trace metal mobility, and redox processes (Cornell and Schwertmann, 2003; Jickells *et al.*, 2005; Boyd and Ellwood, 2010). Hematite (α-Fe_2O_3, space group *R*-3*c*; Figure 1) is the most stable iron oxide phase in moderately to highly oxidizing environments, and because of its abundance and low cost, it is exploited in numerous applications (e.g. photoelectrodes, magnetic materials, anodes for Li batteries) (Cornell and Schwertmann, 2003; Willard *et al.*, 2004; Tartaj *et al.*, 2011; Wang *et al.*, 2012; Wheeler *et al.*, 2012; Bora *et al.*, 2013; Hou *et al.*, 2013; Ma *et al.*, 2013; Reddy *et al.*, 2013; Cheng *et al.*, 2014).

One of the most commonly employed manufacturing protocols for hematite involves crystallization from precursor akaganeite [β-FeO(OH,Cl); space group *I*2/*a*; Figure 2], which has a hollandite-like structure. In akaganeite, edge-linked octahedral chains form tunnels along (010) that are supported by Cl^- or similarly sized anions, such as F^- or OH^- (Weiser and Milligan, 1935; Mackay, 1960; Chambaere and De Grave, 1984; Post and Buchwald, 1991; Cai *et al.*, 2001; Cornell and Schwertmann, 2003; Post *et al.*, 2003a). Based on a Rietveld analysis of powder X-ray diffraction data, Post and Buchwald (1991) report that Cl fills ~2/3 of the tunnel sites. In natural settings, akaganeite primarily forms in Cl-rich environments, such as meteoritic brines, acid mine drainage soils, and metallic iron corrosion sites (Mackay, 1962; Holm *et al.*, 1983; Buchwald and Clarke, 1989;

Refait *et al.*, 1992; Bland *et al.*, 1997; García *et al.*, 2003; Reguer *et al.*, 2007; Gao and Schulze, 2010a, b; Bibi *et al.*, 2011; Fonseca *et al.*, 2012; Masa *et al.*, 2012; Guo and Barnard, 2013; Kampf *et al.*, 2013; Kuebler, 2013). In addition, akaganeite was recently identified in Martian mudstones, where its formation is suggestive of hydrothermal conditions (Grotzinger *et al.*, 2014; McLennan *et al.*, 2014; Ming *et al.*, 2014; Vaniman *et al.*, 2014).

Akaganeite itself offers many technological applications because of its large surface area, non-toxicity, and facile synthesis. For instance, akaganeite has been used as a battery anode, as a catalyst for biomedical applications, as an adsorbent for soil remediation, and for CO_2 capture (Willard *et al.*, 2004; Tabuchi *et al.*, 2009a, b; Dutcher *et al.*, 2011; Lammers *et al.*, 2011; Ali, 2012; Chen *et al.*, 2013; Fütterer *et al.*, 2013; Kou and Varma, 2013; Kumar *et al.*, 2014). Thus, akaganeite synthesis is the focus of much research.

A widely used technique for the precipitation of akaganeite and hematite involves hydrothermal synthesis in ferric chloride solutions (Matijević and Scheiner, 1978; Bailey *et al.*, 1993). The hydrothermal transformation from akaganeite to hematite allows for tailored formation of particles of specific sizes, structures, and morphologies (Wang *et al.*, 2008; Li *et al.*, 2009; Bora *et al.*, 2011; Geng *et al.*, 2012; Yang *et al.*, 2012; Rao *et al.*, 2013). Consequently, much research has focused on the particle size and morphological evolution of akaganeite and hematite particles in the absence and presence of shape-controlling additives.

The details of the hydrothermal structural transformation from akaganeite to hematite are not well documented, and *ex situ* structural analyses may not accurately represent the reaction mechanisms. For example, Peterson *et al.* (2015) described a lower symmetry hematite phase, "monoclinic

---

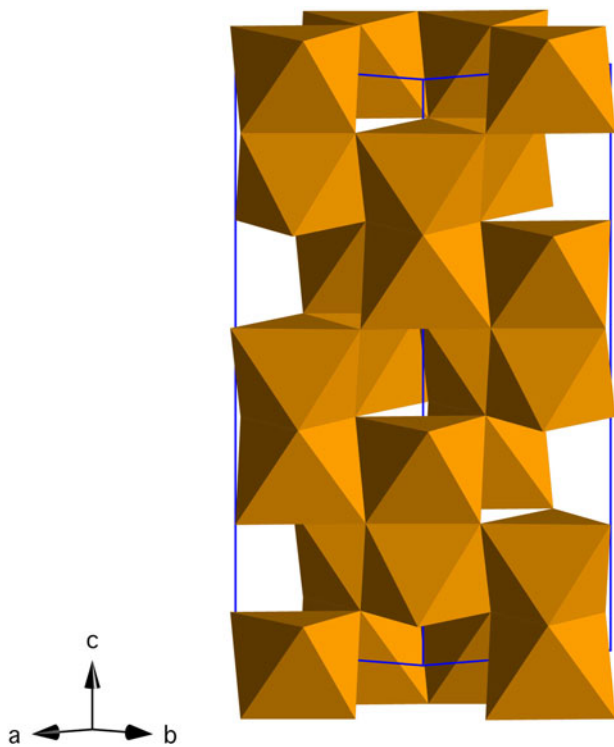a)Author to whom correspondence should be addressed. Electronic mail: k.peterson@hw.ac.uk

Figure 1. (Color online) Crystal structure of hematite (Fe$_2$O$_3$) in the hexagonal setting (R-3c).

hydrohematite" (space group I2/m), from *in situ* hydrothermal time-resolved X-ray diffraction (TR-XRD) experiments at 200 °C. In that study, we were not able to isolate this phase *ex situ*, and we suggested that the stability of monoclinic hydrohematite particles might be extremely sensitive to changes in hydration state and temperature. Thus, the *in situ* nature of our TR-XRD experiments allowed us to capture a

phase that is less accessible through dry heating experiments. Furthermore, the structure of Fe (hydr)oxides can be directly impacted by post-synthesis treatments. For instance, Ellis *et al*. (1976) found that akaganeite specimens are depleted in Cl after washing with water and are more susceptible to electron beam damage when viewed by TEM. Likewise, Ishikawa and Inouye (1975) altered the Cl content of akaganeite specimens by washing with different solutions for variable periods of time.

In Peterson *et al*. (2016), we presented a kinetic analysis of the hydrothermal nucleation and growth of akaganeite and its transformation to hematite. In the present paper, we describe the changes in crystal structure that accompany these reactions using TR-XRD and Rietveld analysis. To our knowledge, this is the first continuous study of the crystallographic changes that occur during the hydrothermal formation of akaganeite and its transformation to hematite. We focused our analyses on a preparation method described by Matijević and Scheiner (1978) for the formation of akaganeite and subsequent hematite transformation to study the effects of temperatures between 100 and 200 °C. We used synchrotron diffraction with a sealed autoclave cell to conduct TR-XRD experiments *in situ*. The data presented are part of a larger study of the transformation of akaganeite to hematite (Peterson *et al*., 2016).

II. EXPERIMENTAL METHODS

A. Sample preparation

All hydrothermal crystallization experiments were performed with solutions containing 0.45 M FeCl$_3$ and 0.01 M HCl, prepared by dilution with deionized water of a 3 M FeCl$_3$ stock solution made with FeCl$_3$ · 6H$_2$O (ACS reagent, JT Baker, Phillipsburg, NJ, USA) and 1 M HCl (ACS reagent, Fisher Scientific, Fair Lawn, NJ, USA) (Matijević and

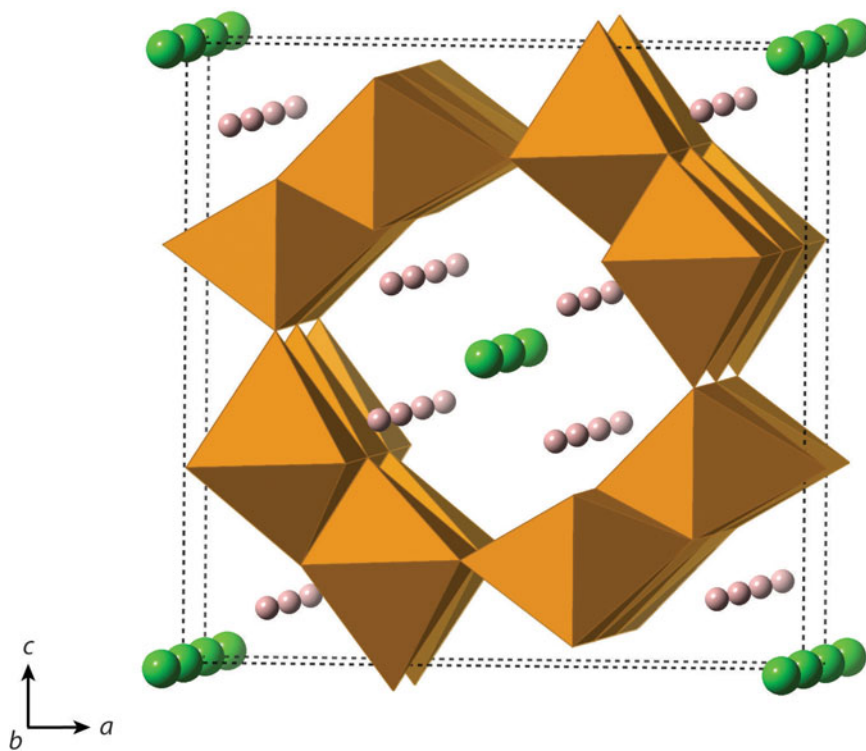Figure 2. (Color online) Crystal structure of akaganeite, β-FeO(OH,Cl) (I2/m). Cl$^-$ is represented by green atoms, and H$^+$ is represented by pink atoms.

Scheiner, 1978). Final solutions were passed through 0.05 μm Millipore filters and stored in sealed Nalgene bottles. For each hydrothermal precipitation experiment, ~7 μl of the 0.45 M $FeCl_3$ solution were loaded into 1.0 mm-outer diameter quartz glass capillaries (Charles Supper Company) and sealed with high-temperature epoxy (302–3 M, Epotek). The reaction vessel can play a major role in determining particle properties and reaction kinetics (Hamada and Matijević, 1982; Kandori et al., 1994; Demopoulos, 2009), and solution volumes, capillary lengths, and amount of headspace were kept as similar as possible to ensure temperature uniformity during heating and to minimize variations among samples. The starting and final pH of the solution was ~1.4 and 1.0, respectively.

B. Synchrotron X-ray diffraction

The *in situ* TR-XRD experiments were conducted at the GeoSoilEnviroCARS (GSECARS) 13-BM-C beamline at the Advanced Photon Source (APS), Argonne National Laboratory (ANL). The X-ray wavelength was 0.8265(8) Å, and the detector distance was 95.165 mm. Because of low precipitate yield during *in situ* experiments, capillaries were tilted at 60° from the horizontal plane to allow for precipitate sedimentation to the bottom of the capillary (Figures 3 and 4). The beam was aimed near the capillary base, enabling the capture of the initial precipitation of akaganeite from solution and the phase transformation to hematite. Each sample was rotated about *Φ* (parallel to the axis of the capillary) by 1° per second during exposure to promote solution mixing and to minimize

Figure 4. (Color online) Experimental setup at APS. (a) The capillary is tilted at a 60° angle from horizontality. (b) The heater is oriented nearly normal to the capillary. The diameter of the outer cylinder sleeve and the capillary length are both ~1 cm to ensure the entire sample volume was heated. A video camera (c) is placed near the capillary to collect video footage of the precipitation of akaganeite and transformation to hematite.
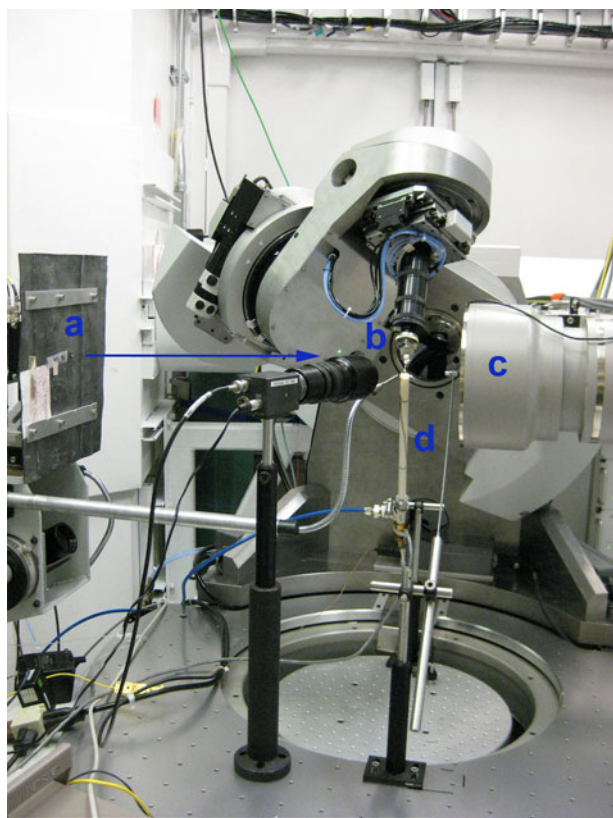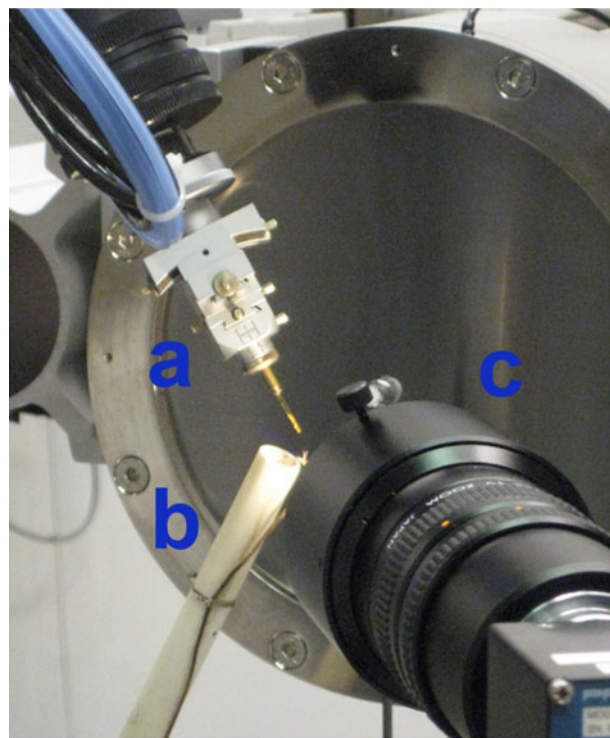

Figure 3. (Color online) Experimental setup at APS. (a) The X-ray beam is aimed at the base of the capillary (b), which is tilted at 60° from the horizontal plane. (c) Area detector. (d) The forced gas heater is positioned beneath the capillary.

preferred orientation effects in the X-ray diffraction patterns. Video images of the capillary solutions revealed vigorous convection of the solutions throughout the heating experiments, suggesting that the solutions were well-mixed and homogeneous.

A forced-gas heater was fabricated at APS by winding Ni coils around an inner ceramic tube with an applied DC voltage using a Sorensen 33 V × 33 A (Model XHR 33-33) power supply to achieve resistive heating. This assembly was encased in an outer ceramic sleeve, and He gas was forced through the interior of the heated cylinder. The diameter of the outer cylinder sleeve and the capillary length were both 1 cm to ensure that the entire sample volume was heated (Figure 4). The heater was oriented approximately normal to the capillary, and a type K chromel–alumel thermocouple was situated adjacent to the capillary and monitored with a Keithly 2700 Multimeter. The actual temperature was calibrated by monitoring two phase transformations of $RbNO_3$ (Alfa Aesar, 99.8%, metals basis) loaded in a 1.0 mm quartz glass capillary and heated from 25.7 to 250 °C. Based on this standardization, we estimate that the temperature measured by the thermocouple was within ±1.5 °C of the actual temperature.

For our experiments, capillary solutions were heated to final temperatures of 100, 150, 175, and 200 °C. Solution heating began after the diffraction pattern of the starting solution at room temperature was completed. Experimental temperatures were reached within 2 min, and were maintained within ±0.25 °C using the EPICS controller software. TR-XRD patterns were collected every 25–40 s using a MAR165 CCD camera for run times ranging from 10 to

160 min. Full-circle images were integrated into intensity vs. 2θ plots using the program Fit2D with a polarization factor of 0.99 (Hammersley *et al.*, 1996). Duplicate runs at temperatures of 150, 175, and 200 °C showed excellent agreement. The similarity in the calculated induction times (39.2 ± 2.8 s) and induction temperatures (122.7 ± 4.5 °C) for experiments between 150 and 200 °C indicated that both the heating rate and solution temperatures were reproducible (Table I).

C. Structure refinement

Rietveld structure refinements were performed using the EXPGUI interface of the General Structures Analysis System (GSAS) program (Toby, 2001; Larson and Von Dreele, 2004). The akaganeite structure parameters were taken from Post *et al.* (2003a). For experiments at 175 °C and below, the *R*-3*c* hematite structure parameters were taken from Blake *et al.* (1966). The monoclinic hydrohematite parameters used in experiments at 200 °C were taken from Peterson *et al.* (2015). Background, scale, peak profile, and unit-cell parameters were initially allowed to vary. Backgrounds were best fitted using a Chebyshev polynomial with 10–12 profile terms. Peak profiles were modeled using a pseudo-Voigt function described by Thompson *et al.* (1987). After these parameters had converged, Fe, O, and Cl atomic positions, hematite Fe occupancies, and akaganeite Cl occupancies were refined. Soft constraints were imposed on akaganeite and monoclinic hydrohematite Fe–O bond lengths.

Akaganeite Fe–O bond lengths were constrained to distances close to those provided in Post and Buchwald (1991) and Post *et al.* (2003a) (1.91–2.15 Å). Soft constraints in the range of 1.90–2.17 Å were imposed on Fe–O bond lengths for monoclinic hydrohematite when both akaganeite and monoclinic hydrohematite phases were present. The bond restraint weighting factor was gradually reduced during the refinements. Lastly, all parameters were allowed to refine simultaneously and the weighting factor was set at to zero, except for akaganeite bond length restraints, which were set to one. Refining isotropic temperature factors generated negative values, and therefore, in all TR-XRD refinements, we fixed temperature factors to those provided in Post *et al.* (2003a) for akaganeite and to those determined from the structure refinement of an *R*-3*c* hematite standard. We prepared this standard using the same ferric chloride solution as was employed for the *in situ* TR-XRD experiments (0.45 M

FeCl$_3$ and 0.01 M HCl). The solution was sealed in a Teflon-lined bomb and heated to 150 °C in a convection oven for 1 h. The final goodness-of-fit parameters for the refinement of the standard hematite were: $\chi^2 = 0.8290$, $R_{wp} = 0.0099$, and $RF^2 = 0.0095$. The 2θ range for all refinements was 15.4° to $\sim$36° (*d*-space range: 1.3–3.1 Å); low-angle data were removed because of the large background scattering from the capillary glass and water. Representative refinements for hydrothermal single-phase akaganeite and hematite as well as a mixed-phase assemblage are presented in Figure 5 and Table II.

The changes in phase abundance, α, were calculated by normalizing GSAS refined scale factors obtained for each phase:

$$\alpha = \frac{S_t}{S_{max}} \tag{1}$$

where S_t is the scale factor at a given time and S_{max} is the maximum scale factor value for the particular experiment. Crystallite size, p (Å), was calculated using Rietveld analysis through the following relation:

$$p = \frac{18\,000\,K\lambda}{\pi X} \tag{2}$$

where K is the Scherrer constant (0.94) and X represents the Lorentzian broadening contribution to peak widths, which is represented in GSAS by the profile parameter "L_x" (Larson and Von Dreele, 2004).

III. RESULTS AND DISCUSSION

We observed the nucleation, growth, and dissolution of akaganeite and transformation to hematite using synchrotron TR-XRD during experiments with temperatures of 150, 175, and 200 °C (Figure 6). At 100 °C, we were able to detect only the nucleation and growth of akaganeite because of the slow transformation kinetics, which can take approximately a week to yield hematite (Matijević and Scheiner, 1978). All induction times, onset of dissolution, and completion of dissolution times are presented in Table I.

A. TR-XRD experiments

As described in Peterson *et al.* (2016), temperature, rather than induction time, drove the nucleation of akaganeite when

TABLE I. Nucleation temperatures, induction and dissolution times, as determined by JMAK kinetic analyses and heater calibration for akaganeite and hematite.

T (°C)	T$_{nuc.}$ (°C)	t$_{heater}$ (s)[a]	Akaganeite crystallization		Akaganeite dissolution		Hematite crystallization
			t$_0$ (s)[b]	t$_{0,\,adj}$ (s)[c]	t$_{\alpha=1}$ (s)	t$_{\alpha=0}$ (s)	t$_0$ (s)[b]
100	100.0(1.5)	47.5	584.5(61)	537	–		–
150 (a)	126.4(1.5)	77.3	119.7(0.3)	42.4	3200	8800	1800(779)
150 (b)	119.2(1.5)	52.8	90.0(0.3)	37.2	–		–
175	123.0(1.5)	52.1	90.0(5.6)	37.9	390	1020	300.0(38.8)
200 (a)	128.7(1.5)	39.6	82.2(5.1)	42.6	175	325	174.8(5.9)
200 (b)	116.4(1.5)	45.7	81.4(0.2)	35.7	150	300	162.5(12.5)
	<122.7(4.5)>[d]			<39.2(2.8)>[d]			

[a]t$_{heater}$: extrapolated time of heater initiation (see Peterson *et al.*, 2016).
[b]t$_0$: induction time calculated from the beginning of XRD data collection ($t = 0$).
[c]t$_{0,\,adj}$: induction time corrected for t$_{heater}$.
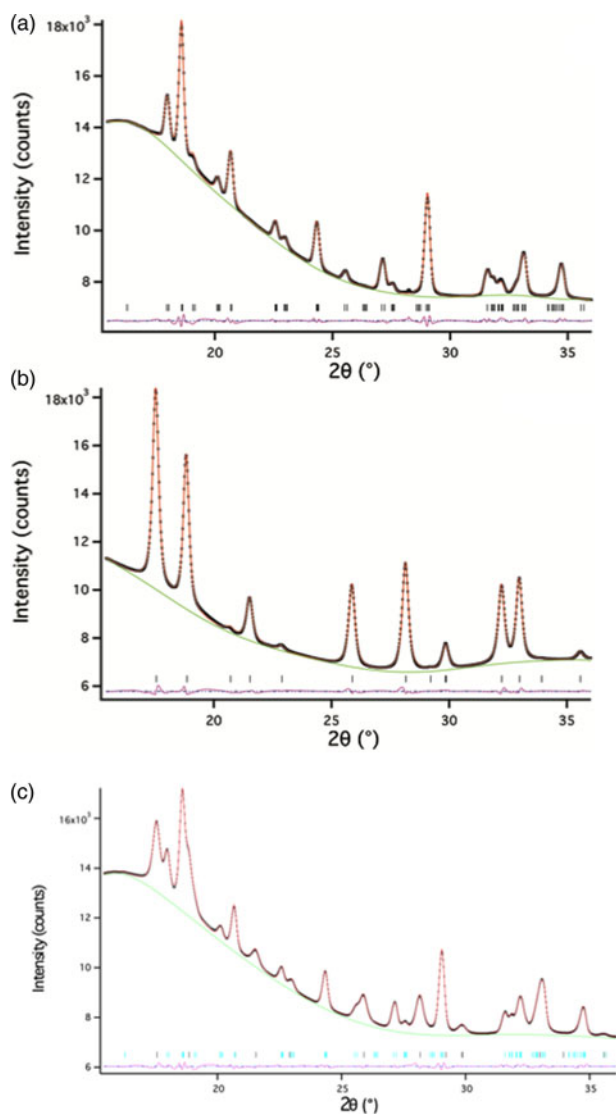[d]Average values of T$_{nuc.}$, t$_{0,\,adj}$ were calculated using 150–200 °C data.

Figure 5. (Color online) Representative Rietveld refinements of (a) akaganeite, (b) hematite, and (c) a mixture of akaganeite and hematite. The data are from an experiment at 175 °C. The data and fits are represented by: observed data (black *x*'s), calculated (red line), differences (pink line), and reflections for each phase (horizontal black lines).

TABLE II. Representative unit-cell parameters and refinement results for akaganeite and hematite.

	Akaganeite	Hematite
	Unit cell	
a (Å)	5.0406(2)	10.5787(11)
b (Å)		3.0351(3)
c (Å)	13.7833(7)	10.5302(11)
β (°)		90.243(8)
V (Å^3)	303.29(3)	338.10(9)
	Cl occupancy	Fe occupancy
	0.992(4)	0.294(10)
	Refinement	
No. of data points	1033	1045
No. of reflections	23	117
Diffraction range (d Å)	15.4–36.07	15.4–36.07
No. of variables	23	44
$R(F^2)$	0.0084	0.0142
R_{wp}	0.0052	0.0040
χ^2	0.2268	0.1688

the temperature was 150 °C or higher. Our TR-XRD data showed that the onset of akaganeite nucleation occurred immediately after the heater attained a temperature of ~123 °C (Table I). This temperature was reached within ~40 s for all samples. For our experiments at 100 °C, which is below the 123 °C threshold, the induction time for akaganeite nucleation was 9 min.

Hematite nucleation was first detected just before or coincident with the onset of akaganeite dissolution at all temperatures. The refined akaganeite phase abundances attained between 98 and 100 wt% of their maximum values at the moment of the first detectable hematite precipitation. On the other hand, the complete dissolution of akaganeite seemed to be closely related to temperature. At 200 °C, akaganeite was fully dissolved at an earlier stage relative to the abundance of hematite than at 150 and 175 °C. Specifically, during the experiments at 150 and 175 °C, akaganeite was no longer detected when hematite reached ~85% of its ultimate abundance. During the 200 °C experiment, however, akaganeite had disappeared once the hematite phase abundance reached 57 wt% of its final abundance. Our kinetic analyses reported in Peterson et al. (2016) revealed that the rate constants of akaganeite dissolution and hematite precipitation were approximately equal during the experiments at 150 and 175 °C. However, at 200 °C, the rate of akaganeite dissolution was twice as large as the rate of hematite precipitation.

B. Structural changes during crystallization and dissolution

Rietveld analyses of time-resolved data showed that unit-cell parameters varied with temperature and with extent of reaction, although the changes in unit-cell parameters were subtle (Figures 7–10). The data points in these graphs are larger than the errors reported by GSAS, but as concentrations diminished, the peak-to-background intensities decreased and the real error is suggested by the scatter in the data. Since the XRD patterns with abundances below 5 wt% could not be reliably refined, only unit-cell data for akaganeite and hematite phase abundances above ~5 wt% are included. For purposes of comparison, the monoclinic unit-cell parameters for the hydrohematite generated at 200 °C are recast using a pseudo-hexagonal unit cell.

1. Structural changes during crystallization and dissolution of akaganeite

Akaganeite nanocrystals exhibited measurable structural changes following nucleation, and again after the onset of dissolution. At all temperatures (100–200 °C), the first akaganeite crystallite diameters were ~30 nm. The akaganeite *a*- and *c*-axes contracted and the *b*-axis increased during crystal growth, and this behavior continued even into the early stages of akaganeite dissolution (with <10 wt% of the akaganeite dissolved) (Figures 7 and 8). The contractions of *a* and *c* were counterbalanced by the expansion of *b*, and the unit-cell volume was constant within an error at 100 °C and decreased only by up to ~0.3% for the higher temperature runs. The Cl occupancy for the first particles for which refinement was feasible was ~0.2, and that value slightly increased and stabilized at ~0.3 for all temperatures.
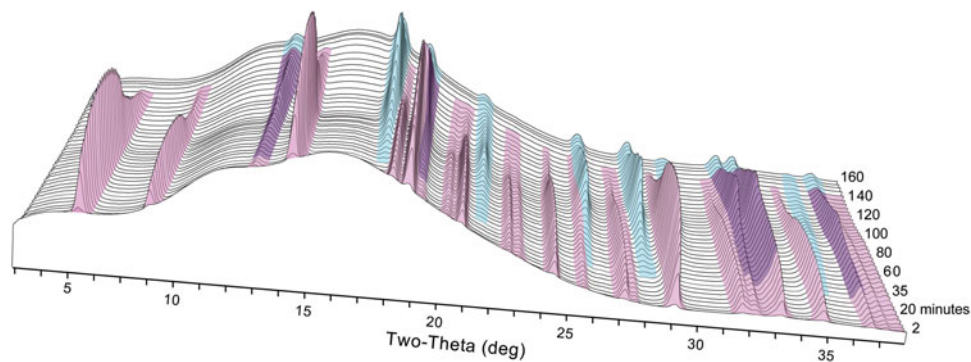
Figure 6. (Color online) Representative time series of X-ray diffraction patterns collected at 150 °C. Akaganeite peaks are colored pink, and hematite peaks are colored blue.
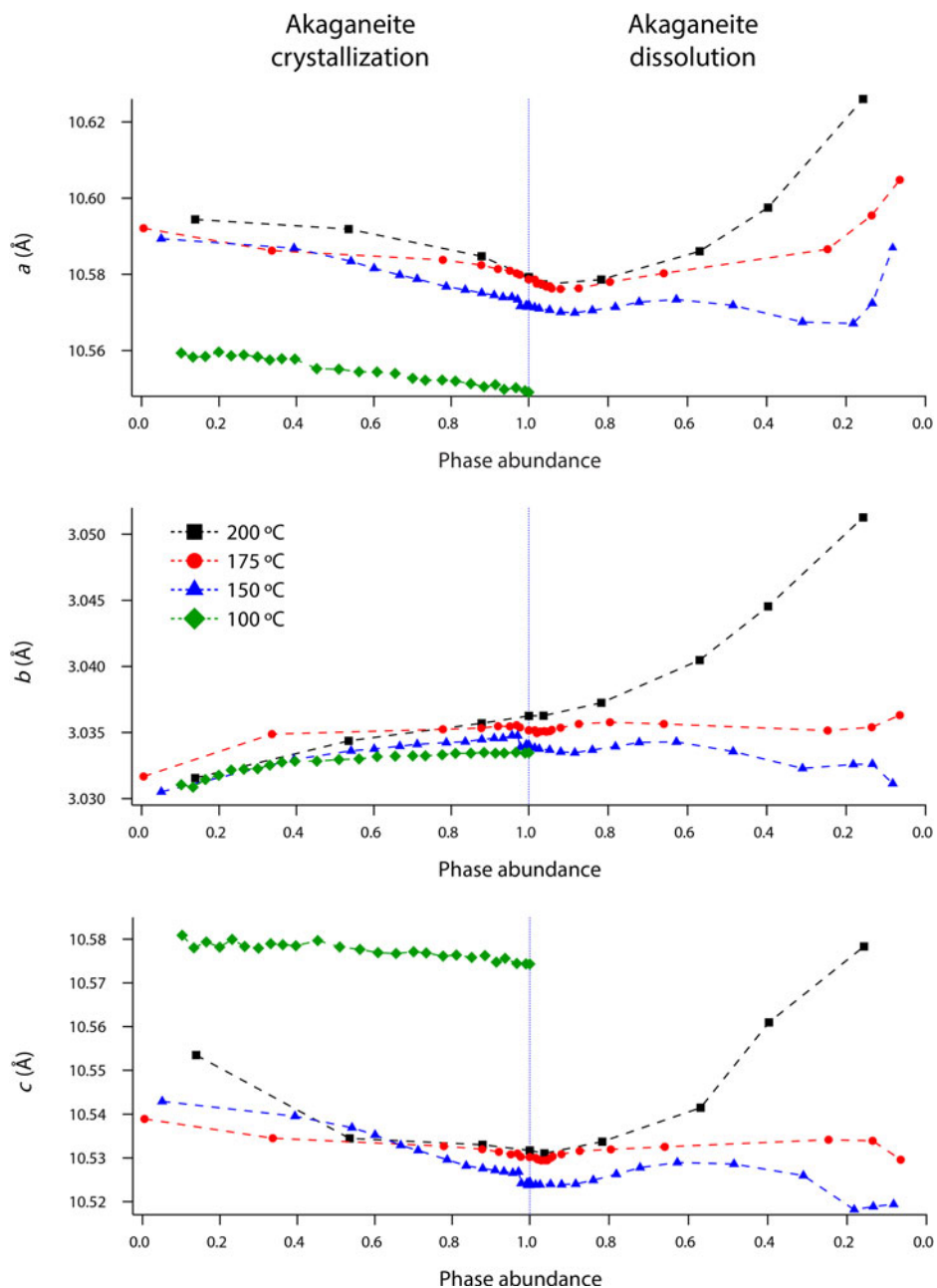

Figure 7. (Color online) Changes in akaganeite a, b, and c at 100 (green diamonds), 150 (blue triangles), 175 (red circles), and 200 °C (black squares) as a function of akaganeite phase abundance.

Figure 8. (Color online) Changes in akaganeite β, volume, and Cl occupancy at 100 (green diamonds), 150 (blue triangles), 175 (red circles), and 200 °C (black squares) as a function of akaganeite phase abundance.
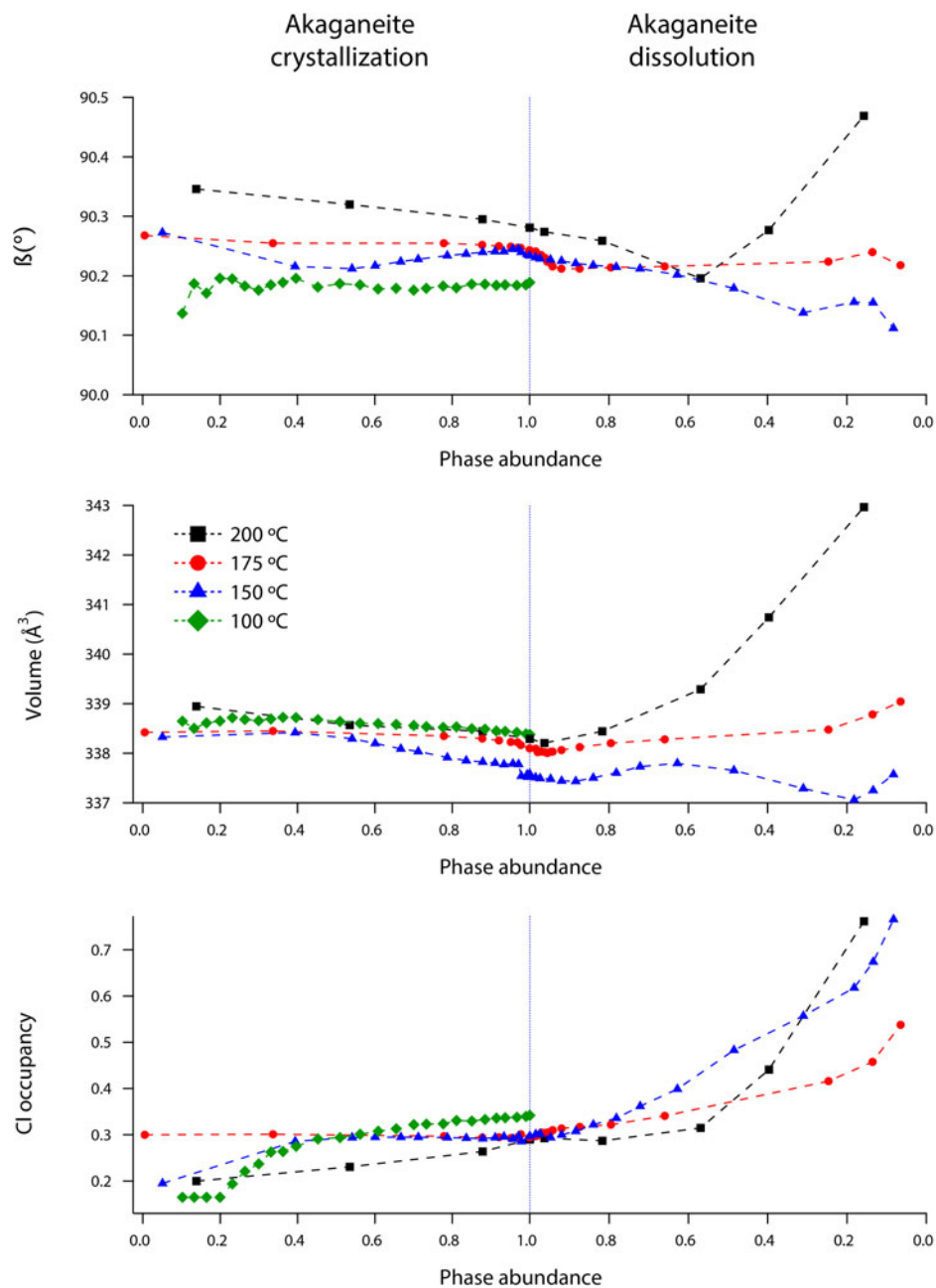
Interestingly, dissolution was marked by a more significant structural evolution: the unit-cell volume increased as all of the unit-cell edge lengths slightly expanded. One explanation for this volume increase may be tied to an unexpected change in the fractional occupancy of the Cl site within the tunnels. As the akaganeite dissolved, the refined occupancy of Cl in the tunnels increased dramatically from ∼0.3 to an average final refined occupancy of 0.75 ± 0.02, and manually lowering the Cl occupancy worsened the fit. For example, for a refined Cl occupancy of 0.71, $RF^2 = 0.0137$, whereas a forced Cl occupancy of 0.3 for the late-stage dissolution of akaganeite yielded a higher RF^2 of 0.0272. The refined Cl occupancy of ∼0.3 for akaganeite before the onset of dissolution is very close to the value of 0.34 reported for akaganeite in a meteoritic corrosion crust (Post and Buchwald, 1991).

This Cl concentration agrees well with the value of 1.25 Cl per unit cell that Post and Buchwald (1991) measured by electron probe microanalysis.

The Cl anions are located within the hollandite-like tunnels of akaganeite, displaced slightly from (0,0,0), and an occupancy of 0.34 indicates that roughly two-thirds of the tunnel sites are occupied. A subsequent study of the same sample using neutron diffraction (Post et al., 2003a) yielded a slightly higher Cl occupancy (0.42, or ∼1.6 Cl anions per unit cell), but the authors discounted this refined value based on the effects that different isotopes of Cl would exert on neutron scattering. Thus, our refined occupancy for Cl when akaganeite was at its most abundant in our experiments (∼0.30) matches well with the most reliable published measurement for a natural specimen.
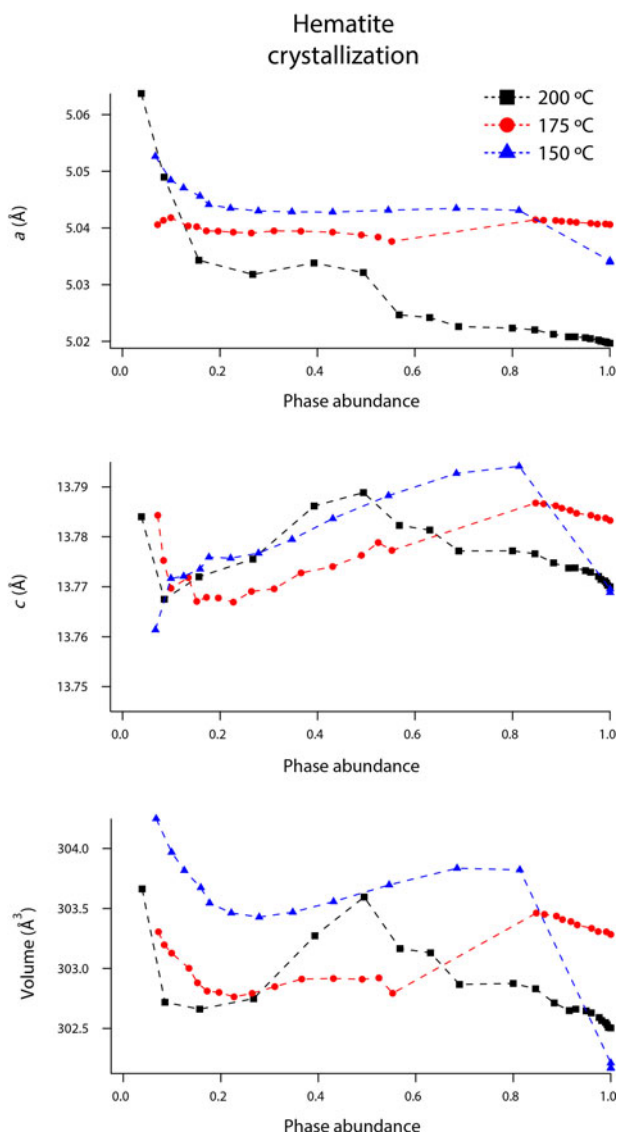
Hematite crystallization

Figure 9. (Color online) Changes in hematite *a*, *c*, and volume at 150 (blue triangles), 175 (red circles), and 200 °C (black squares) as a function of hematite phase abundance.

Hematite crystallization

Figure 10. (Color online) Changes in hematite *c/a* and Fe occupancy at 150 (blue triangles), 175 (red circles), and 200 °C (black squares) as a function of hematite phase abundance.

A refined value of 0.5 for the occupancy of Cl indicates that all of the tunnel sites are filled. Thus, as akaganeite dissolved (and the particles were smaller), Cl might have preferentially fractionated into the crystal rather than the fluid up to the theoretical limit of what akaganeite could accommodate. However, our refined Cl occupancies were consistently greater than the theoretical limit of 0.5 during akaganeite dissolution. Ishikawa and Inouye (1975) suggested that water might partially replace Cl within the akaganeite tunnel. Previous studies using IR spectroscopy and XRD only revealed trace quantities of water molecules existing within the tunnel sites (Keller, 1970; Post and Buchwald, 1991; Post et al., 2003a). In their neutron diffraction study, Post et al. (2003a) determined that the three H sites were partially occupied, with fractions ranging from 0.3 to 0.5. An increase in Cl during dissolution would have to be accompanied by a concomitant increase in the H content of the final akaganeite nanocrystals to maintain charge balance, since our refinements did not reveal a decrease in the occupancy of the Fe sites.
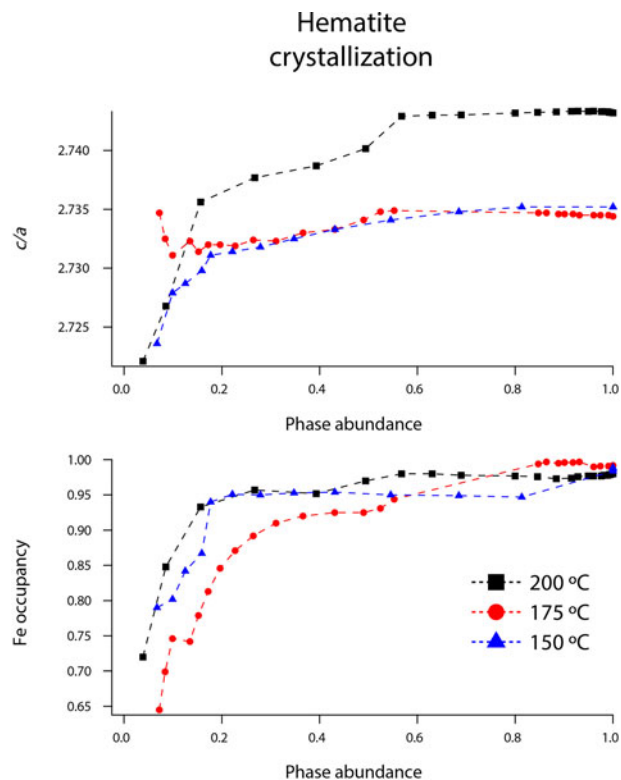
In light of the refined values for Cl occupancy beyond the theoretical limit, another explanation may involve Fe migration into tunnel sites during akaganeite dissolution. For example, Post et al. (2003b) examined the thermal decomposition of the Mn oxide todorokite, which has a 3×3 octahedral tunnel structure, and they found strong evidence that Mn migrates into todorokite tunnel sites during its thermal decomposition to the closest-packed hausmannite structure. Perhaps as akaganeite transforms to the closest-packed hematite structure, Fe^{3+} cations similarly migrate to tunnel sites as an intermediate step in the framework reconstruction, presumably with the loss of H to maintain charge balance.

2. Fe–O bond behavior

Akaganeite has two distinct Fe1 and Fe2 octahedral sites, each having three shorter Fe–O bonds and three longer Fe–OH bonds. Based on Rietveld analysis of neutron diffraction data, Post et al. (2003a) calculated Fe–O bond lengths of 1.944–1.985 Å for the shorter bonds, and Fe–OH bond lengths of 2.054–2.130 Å for the longer bonds. Their average Fe–(O, OH) bond length is 2.01 Å for the Fe1 site and 2.05 Å for the Fe2 site.

Our refined akaganeite bond lengths were in good agreement with those of Post et al. (2003a). During crystallization, the average Fe1–OH and Fe1–O bond lengths increased by ~0.03 Å (from 2.08 to 2.11 Å and 1.98 to 2.01 Å, respectively) as the akaganeite abundance approached its maximum value. These values were consistent for all temperatures. Also during crystallization, the Fe2–OH distances decreased by ~0.02 Å, and Fe2–O bond lengths decreased by ~0.04 Å.

During dissolution, average Fe1–OH and Fe1–O distances decreased by 0.03 and 0.04 Å, respectively. The Fe2–OH distances decreased by ~0.02 Å, and Fe2–O bond lengths increased by ~0.05 Å. Our Cl–Cl distances remained ~3.035 Å, regardless of the Cl occupancy and refined Cl anion positions. This value is lower than the expected distance of ~3.8 Å, but similar to the distance of 3.03 Å determined by Post and Buchwald (1991).

3. Structural changes during the growth of hematite

Hematite is hexagonal with space group R-$3c$ (Figure 1). The structure contains a framework of hexagonally closest packed O^{2-} anions along (001), and Fe^{3+} cations occupy two-thirds of the octahedral interstices (Blake et al., 1966; Cornell and Schwertmann, 2003). When hematite forms in solution or via an iron oxyhydroxide intermediate, it can retain variable amounts of water and OH groups within its structure. The water and OH groups substitute for O^{2-} anions, and are accompanied by Fe vacancies for charge balance. These hydrated hematite phases are often referred to as "protohematite" or "hydrohematite" (Wolska, 1981; Wolska and Schwertmann, 1989; Dang et al., 1998; Gualtieri and Venturelli, 1999; Burgina et al., 2000a, b).

Our refined unit-cell parameters for the growing particles of hematite are consistent with the initial formation of OH-rich, Fe-deficient hematite phases at all temperatures. During the experiments at 150, 175, and 200 °C, the hematite a-axes contracted throughout the experiments (Figures 9 and 10). The hematite c-axes expanded until the late stages of akaganeite dissolution (~60% of akaganeite dissolved), and then the c-axes contracted during the rest of the experiment. The coupled a- and c-axis contraction is frequently described in the protohematite and hydrohematite literature, and is explained as a consequence of OH loss and filling of Fe vacancies (Dang et al., 1998; Cornell and Schwertmann, 2003). The replacement of vacancies by Fe with increasing particle size and maturity is also reflected in the increase in refined Fe occupancies from an average of 0.72 to nearly full occupancy. If H^+ is charge balancing the Fe^{3+} deficiencies, then the water content for the initial crystals of hematite in our experiments was ~12 wt%, which is similar to that of akaganeite and goethite (Cornell and Schwertmann, 2003; Post et al., 2003a).

The structure of hematite consists of trigonally distorted octahedra, which contain three longer Fe–O face-sharing bond lengths (2.116 Å) and three shorter unshared Fe–O bond lengths (1.945 Å) (Blake et al., 1966). Fe–Fe distances (2.900 Å) between face-sharing octahedra along c are shorter than edge-sharing octahedral Fe–Fe distances (2.971 Å) within the octahedral layers. At all temperatures, Fe–O face-sharing bond lengths increased and unshared Fe–O bond lengths decreased throughout the experiments.

On the other hand, Fe–Fe distances between face-sharing octahedra increased during our experiments at 200 °C, but they decreased when crystals evolved at 150 and 175 °C. We believe this difference is real and not attributable to experimental artifacts, as it was reproduced in duplicate experiments. Most likely, this behavior is linked to the formation of a lower symmetry hematite phase during our 200 °C experiments, as indicated by distinct peak splitting in our diffraction data. In our recent study, we presented a refined structure for this phase, described as monoclinic hydrohematite (space

group $I2/m$) (Peterson et al., 2015). Monoclinic hydrohematite was not evident in our 150 and 175 °C experiments, although the concentrations of Fe vacancies were similar at all temperatures. Peterson et al. (2015) attribute the monoclinic phase to the accelerated reaction kinetics at 200 °C.

IV. CONCLUSION

We used TR-XRD to track the hydrothermal nucleation and growth of akaganeite and its transformation to hematite during in situ experiments between 100 and 200 °C. During the crystallization of akaganeite, our Rietveld analyses demonstrated that the unit-cell volume remained essentially constant, with a small (0.3%) contraction at the higher temperatures. Cl occupancy increased from 0.2 and stabilized at 0.3. However, the onset of akaganeite dissolution and hematite precipitation was accompanied by a reversal of these trends. The akaganeite unit cell expanded and Cl occupancy rapidly increased to ~0.72, greater than the theoretical limit of 0.5. We suggest that Cl sites might be partially filled by Fe^{3+} migration into the tunnel during the breakdown of the akaganeite structure as it transforms to hematite. Rietveld analyses supported the incipient formation of an OH-rich, Fe-deficient hydrohematite that over timescales of minutes evolved to stoichiometric hematite. We suggest that these transformations describe the crystallographic maturation of akaganeite and hematite in both synthetic and natural hydrothermal systems.

Ali, I. (2012). "New generation adsorbents for water treatment," Chem. Rev. 112, 5073–5091.

Bailey, J. K., Brinker, C. J., and Mecartney, M. L. (1993). "Growth mechanisms of iron oxide particles of differing morphologies from the forced hydrolysis of ferric chloride solutions," J. Colloid Interface Sci. 157, 1–13.

Bibi, I., Singh, B., and Silvester, E. (2011). "Akaganéite (β-FeOOH) precipitation in inland acid sulfate soils of south-western New South Wales (NSW), Australia," Geochim. Cosmochim. Acta 75, 6429–6438.

Blake, R. L., Hessevick, R. E., Zoltai, T., and Finger, L. W. (1966). "Refinement of the hematite structure," Am. Mineral. 51, 123–129.

Bland, P. A., Kelley, S. P., Berry, F. J., Cadogan, J. M., and Pillinger, C. T. (1997). "Artificial weathering of the ordinary chondrite Allegan: implications for the presence of Cl as a structural component in akaganeite," Am. Mineral. 82, 1187–1197..

Bora, D. K., Braun, A., Erni, R., Fortunato, G., Graule, T., and Constable, E. C. (2011). "Hydrothermal treatment of a hematite film leads to highly

oriented faceted nanostructures with enhanced photocurrents," Chem. Mater. **23**, 2051–2061.

Bora, D. K., Braun, A., and Constable, E. C. (**2013**). "'In rust we trust.' Hematite – the prospective inorganic backbone for artificial photosynthesis," Energy Environ. Sci. **6**, 407–425.

Boyd, P. W. and Ellwood, M. J. (**2010**). "The biogeochemical cycle of iron in the ocean," Nat. Geosci. **3**, 675–682.

Buchwald, V. F. and Clarke, R. S. J. (**1989**). "Corrosion of Fe–Ni alloys by Cl-containing akaganéite (beta-FeOOH): the Antarctic meteorite case," Am. Mineral. **74**, 656–667.

Burgina, E. B., Kustova, G. N., Isupova, L. A., Tsybulya, S. V., Kryukova, G. N., and Sadykov, V. A. (**2000a**). "Investigation of the structure of proto-hematite – metastable phase of ferrum (III) oxide," J. Mol. Catal. A Chem. **158**, 257–261.

Burgina, E. B., Kustova, G. N., Tsybulya, S. V., Kryukova, G. N., Litvak, G. S., Isupova, L. A., and Sadykov, V. A. (**2000b**). "Structure of the metastable modification of iron (III) oxide," J. Struct. Chem. **41**, 396–402.

Cai, J., Liu, J., Gao, Z., Navrotsky, A., and Suib, S. L. (**2001**). "Synthesis and anion exchange of tunnel structure akaganeite," Chem. Mater. **13**, 4595–4602.

Chambaere, D. G. and De Grave, E. (**1984**). "A study of the non-stoichiometrical halogen and water content of β-FeOOH," Phys. Status Solidi A **83**, 93–102.

Chen, M. L., Shen, L. M., Chen, S., Wang, H., Chen, X. W., and Wang, J. H. (**2013**) "In situ growth of β-FeOOH nanorods on graphene oxide with ultra-high relaxivity for in vivo magnetic resonance imaging and cancer therapy," J. Mater. Chem. B **1**, 2582–2589.

Cheng, X. L., Jiang, J. S., Jin, C. Y., Lin, C. C., Zeng, Y., and Zhang, Q. H. (**2014**). "Cauliflower-like α-Fe$_2$O$_3$ microstructures: toluene–water interface-assisted synthesis, characterization, and applications in wastewater treatment and visible-light photocatalysis," Chem. Eng. J. **236**, 139–148.

Cornell, R. M. and Schwertmann, U. (**2003**). *The Iron Oxides: Structure, Properties, Reactions, Occurrences and Uses* (WILEY-VCH Verlag GmbH & Co. KGaA, Weinheim).

Dang, M. Z., Rancourt, D. G., Dutrizac, J. E., Lamarche, G., and Provencher, R. (**1998**). "Interplay of surface conditions, particle size, stoichiometry, cell parameters, and magnetism in synthetic hematite-like materials," Hyperfine Interact. **117**, 271–319.

Demopoulos, G. P. (**2009**). "Aqueous precipitation and crystallization for the production of particulate solids with desired properties," Hydrometallurgy **96**, 199–214.

Dutcher, B., Fan, M., Leonard, B., Dyar, M. D., Tang, J., Speicher, E. A., Liu, P., and Zhang, Y. (**2011**). "Use of nanoporous FeOOH as a catalytic support for NaHCO$_3$ decomposition aimed at reduction of energy requirement of Na$_2$CO$_3$/NaHCO$_3$ based CO$_2$ separation technology," J. Phys. Chem. C **115**, 15532–15544.

Ellis, J., Giovanoli, R., and Stumm, W. (**1976**). "Anion-exchange properties of β-FeOOH," Chimia **30**, 194–197.

Fonseca, M. C., Bastos, I. N., Baggio-Saitovitch, E., and Sánchez, D. R. (**2012**). "Characterization of oxides of stainless steel UNS S30400 formed in offshore environment," Corros. Sci. **55**, 34–39.

Fütterer, S., Andrusenko, I., Kolb, U., Hofmeister, W., and Langguth, P. (**2013**). "Structural characterization of iron oxide/hydroxide nanoparticles in nine different parenteral drugs for the treatment of iron deficiency anaemia by electron diffraction (ED) and X-ray powder diffraction (XRPD)," J. Pharm. Biomed. Anal. **86**, 151–160.

Gao, X. and Schulze, D. G. (**2010a**). "Chemical and mineralogical characterization of arsenic, lead, chromium, and cadmium in a metal-contaminated Histosol," Geoderma **156**, 278–286.

Gao, X. and Schulze, D. G. (**2010b**). "Precipitation and transformation of secondary Fe oxyhydroxides in a Histosol impacted by runoff from a lead smelter," Clays Clay Miner. **58**, 377–387.

García, K. E., Morales, A. L., Arroyave, C. E., Barrero, C. A., and Cook, D. C. (**2003**). "Mössbauer characterization of rust obtained in an accelerated corrosion test," Hyperfine Interact. **148**, 177–183.

Geng, B., Tao, B., Li, X., and Wei, W. (**2012**). "Ni^{2+}/surfactant-assisted route to porous α-Fe$_2$O$_3$ nanoarchitectures," Nanoscale **4**, 1671–1676.

Grotzinger, J. P., Sumner, D. Y., Kah, L. C., Stack, K., Gupta, S., Edgar, L., Rubin, D., Lewis, K., Schieber, J., and Mangold, N. (**2014**). "A habitable fluvio-lacustrine environment at Yellowknife Bay, Gale Crater, Mars," Science **343**, 1242777.

Gualtieri, A. F. and Venturelli, P. (**1999**). "In situ study of the goethite-hematite phase transformation by real time synchrotron powder diffraction," Am. Mineral. **84**, 895–904.

Guo, H. and Barnard, A. S. (**2013**). "Naturally occurring iron oxide nanoparticles: morphology, surface chemistry and environmental stability," J. Mater. Chem. A **1**, 27–42.

Hamada, S. and Matijević, E. (**1982**). "Formation of monodispersed colloidal cubic haematite particles in ethanol + water solutions," J. Chem. Soc. Faraday Trans. 1 **78**, 2147–2156.

Hammersley, A. P., Svensson, S. O., Hanfland, M., Fitch, A. N., and Hausermann, D. (**1996**). "Two-dimensional detector software: from real detector to idealised image or two-theta scan," High Press. Res. **14**, 235–248.

Holm, N. G., Dowler, M. J., Wadsten, T., and Arrhenius, G. (**1983**). "B-FeOOH · Cl$_n$ (akaganéite) and Fe$_{1−x}$O (wüstite) in hot brine from the Atlantis II Deep (Red Sea) and the uptake of amino acids by synthetic β-FeOOH···Cl$_n$," Geochim. Cosmochim. Acta **47**, 1465–1470.

Hou, Y., Wang, D., Yang, X. H., Fang, W. Q., Zhang, B., Wang, H. F., Lu, G. Z., Hu, P., Zhao, H. J., and Yang, H. G. (**2013**). "Rational screening low-cost counter electrodes for dye-sensitized solar cells," Nat. Commun. **4**, 1583.

Ishikawa, T. and Inouye, K. (**1975**). "Role of chlorine in β-FeOOH on its thermal change and reactivity to sulfur dioxide," Bull. Chem. Soc. Jpn. **48**, 1580–1584.

Jickells, T. D., An, Z. S., Andersen, K. K., Baker, A. R., Bergametti, G., Brooks, N., Cao, J. J., Boyd, P. W., Duce, R. A., and Hunter, K. A. (**2005**). "Global iron connections between desert dust, ocean biogeochemistry, and climate," Science **308**, 67–71.

Kampf, A. R., Mills, S. J., Nestola, F., Ciriotti, M. E., and Kasatkin, A. V. (**2013**). "Saltonseaite, K$_3$NaMn^{2+}Cl$_6$, the Mn analogue of rinneite from the Salton Sea, California," Am. Mineral. **98**, 231–235.

Kandori, K., Tamura, S., and Ishikawa, T. (**1994**). "Inner structure and properties of diamond-shaped and spherical α-Fe$_2$O$_3$ particles," Colloid Polym. Sci. **27**, 812–819.

Keller, P. (**1970**). "Eigenschaften von (Cl,F,OH)$_{<2}$Fe$_8$(O,OH)$_{16}$ und Akaganeite," Neu. Jb. Mineral. Abh. **113**, 29–49.

Kou, J. and Varma, R. S. (**2013**). "Expeditious organic-free assembly: morphologically controlled synthesis of iron oxides using microwaves," Nanoscale **5**, 8675–8679.

Kuebler, K. E. (**2013**). "A comparison of the iddingsite alteration products in two terrestrial basalts and the Allan Hills 77005 Martian meteorite using Raman spectroscopy and electron microprobe analyses," J. Geophys. Res. Planets **118**, 803–830.

Kumar, E., Bhatnagar, A., Hogland, W., Marques, M., and Sillanpää, M. (**2014**). "Interaction of inorganic anions with iron-mineral adsorbents in aqueous media – a review," Adv. Colloid Interface Sci. **203**, 11–21.

Lammers, K., Murphy, R., Riendeau, A., Smirnov, A., Schoonen, M. A. A., and Strongin, D. R. (**2011**). "CO$_2$ sequestration through mineral carbonation of iron oxyhydroxides," Environ. Sci. Technol. **45**, 10422–10428.

Larson, A. C. and Von Dreele, R. B. (**2004**). *General Structure Analysis System (GSAS)* (Report LAUR 86-748). Los Alamos, New Mexico: Los Alamos National Laboratory.

Li, X., Yu, X., He, J., and Xu, Z. (**2009**). "Controllable fabrication, growth mechanisms, and photocatalytic properties of hematite hollow spindles," J. Phys. Chem. C **113**, 2837–2845.

Ma, J., Zhang, X., Chen, K., Li, G., and Han, X. (**2013**). "Morphology-controlled synthesis of hematite hierarchical structures and their lithium storage performances," J. Mater. Chem. A **1**, 5545–5553.

Mackay, A. L. (**1960**). "β-ferric oxyhydroxide," Mineral. Mag. **32**, 545–557.

Mackay, A. L. (**1962**). "β-ferric oxyhydroxide – akaganeite," Mineral. Mag. **33**, 270–280.

Masa, B., Pulisova, P., Bezdicka, P., Michalkova, E., and Subrt, J. (**2012**). "Ochre precipitates and acid mine drainage in a mine environment," Ceram. Silik. **56**, 9–14.

Matijević, E. and Scheiner, P. (**1978**). "Ferric hydrous oxide sols: III. Preparation of uniform particles by hydrolysis of Fe (III)-chloride, -nitrate, and -perchlorate solutions," J. Colloid Interface Sci. **63**, 509–524.

McLennan, S. M., Anderson, R. B., Bell, J. F., Bridges, J. C., Calef, F., Campbell, J. L., Clark, B. C., Clegg, S., Conrad, P., and Cousin, A. (**2014**). "Elemental geochemistry of sedimentary rocks at Yellowknife Bay, Gale Crater, Mars," Science **343**, 1244734.

Ming, D. W., Archer, P. D., Glavin, D. P., Eigenbrode, J. L., Franz, H. B., Sutter, B., Brunner, A. E., Stern, J. C., Freissinet, C., and McAdam, A. C.

(2014). "Volatile and organic compositions of sedimentary rocks in Yellowknife Bay, Gale Crater, Mars," Science **343**, 1245267.

Peterson, K. M., Heaney, P. H., Post, J. E., and Eng, P. J. (**2015**). "A refined monoclinic structure for a high-temperature 'hydrohematite'," Am. Mineral. **100**, 570–579.

Peterson, K. M., Heaney, P. H., and Post, J. E. (**2016**). "A kinetic analysis of the transformation from akaganeite to hematite: an *in situ* time-resolved X-ray diffraction study," Chem. Geol. **444**, 27–36.

Post, J. E. and Buchwald, V. F. (**1991**). "Crystal structure refinement of akaganeite," Am. Mineral. **76**, 272–277.

Post, J. E., Heaney, P. J., Von Dreele, R. B., and Hanson, J. C. (**2003a**). "Neutron and temperature-resolved synchrotron X-ray powder diffraction study of akaganeite," Am. Mineral. **88**, 782–788.

Post, J. E., Heaney, P. J., and Hanson, J. (**2003b**). "Synchrotron X-ray diffraction study of the structure and dehydration behavior of todorokite," Am. Mineral. **88**, 142–150.

Rao, X., Su, X., Yang, C., Wang, J., Zhen, X., and Ling, D. (**2013**). "From spindle-like β-FeOOH nanoparticles to α-Fe_2O_3 polyhedral crystals: shape evolution, growth mechanism and gas sensing property," CrystEngComm **15**, 7250–7256.

Reddy, M. V., Subba Rao, G. V., and Chowdari, B. V. R. (**2013**). "Metal oxides and oxysalts as anode materials for Li ion batteries," Chem. Rev. **113**, 5364–5457.

Refait, P., Ouahman, R., Forrières, C., and Génin, J. M. R. (**1992**). "The role of Cl^- ions in the oxidation of iron artifacts from chlorinated archeological environments," Hyperfine Interact. **70**, 997–1000.

Reguer, S., Dillmann, P., and Mirambet, F. (**2007**). "Buried iron archaeological artefacts: corrosion mechanisms related to the presence of Cl-containing phases," Corros. Sci. **49**, 2726–2744.

Tabuchi, T., Katayama, Y., Nukuda, T., and Ogumi, Z. (**2009a**). "β-FeOOH thin film as positive electrode for lithium-ion cells," J. Power Sources **191**, 640–643.

Tabuchi, T., Katayama, Y., Nukuda, T., and Ogumi, Z. (**2009b**). "Surface reaction of β-FeOOH film negative electrode for lithium-ion cells," J. Power Sources **191**, 636–639.

Tartaj, P., Morales, M. P., Gonzalez-Carreño, T., Veintemillas-Verdaguer, S., and Serna, C. J. (**2011**). "The iron oxides strike back: from biomedical applications to energy storage devices and photoelectrochemical water splitting," Adv. Mater. **23**, 5243–5249.

Thompson, P., Cox, D. E., and Hastings, J. B. (**1987**). "Rietveld refinement of Debye–Scherrer synchrotron X-ray data from Al_2O_3," J. Appl. Crystallogr. **20**, 79–83.

Toby, B. H. (**2001**). "EXPGUI, a graphical user interface for GSAS," J. Appl. Crystallogr. **34**, 1–4.

Vaniman, D. T., Bish, D. L., Ming, D. W., Bristow, T. F., Morris, R. V., Blake, D. F., Chipera, S. J., Morrison, S. M., Treiman, A. H., Rampe, E. B., Rice, M., Achilles, C. N., Grotzinger, J. P., McLennan, S. M., Williams, J., Bell, J. F., Newsom, H. E., Downs, R. T., Maurice, S., Sarrazin, P., Yen, A. S., Morookian, J. M., Farmer, J. D., Stack, K., Milliken, R. E., Ehlmann, B. L., Sumner, D. Y., Berger, G., Crisp, J. A., Hurowitz, J. A., Anderson, R., Des Marais, D. J., Stolper, E. M., Edgett, K. S., Gupta, S., and Spanovich, N., MSL Science Team (**2014**). "Mineralogy of a mudstone at Yellowknife Bay, Gale Crater, Mars," Science **343**, 1243480.

Wang, B., Chen, J. S., and Lou, X. W. D. (**2012**). "The comparative lithium storage properties of urchin-like hematite spheres: hollow vs. solid," J. Mater. Chem. **22**, 9466–9468.

Wang, D., Song, C., Zhao, Y., and Yang, M. (**2008**). "Synthesis and characterization of monodisperse iron oxides microspheres," J. Phys. Chem. C **112**, 12710–12715.

Weiser, H. B. and Milligan, W. O. (**1935**). "X-ray studies on the hydrous oxides. V. Beta ferric oxide monohydrate," J. Am. Chem. Soc. **57**, 238–241.

Wheeler, D. A., Wang, G., Ling, Y., Li, Y., and Zhang, J. Z. (**2012**). "Nanostructured hematite: synthesis, characterization, charge carrier dynamics, and photoelectrochemical properties," Energy Environ. Sci. **5**, 6682–6702.

Willard, M. A., Kurihara, L. K., Carpenter, E. E., Calvin, S., and Harris, V. G. (**2004**). "Chemically prepared magnetic nanoparticles," Int. Mater. Rev. **49**, 125–170.

Wolska, E. (**1981**). "The structure of hydrohematite," Z. Kristallogr. **154**, 69–75.

Wolska, E. and Schwertmann, U. (**1989**). "Nonstoichiometric structures during dehydroxylation of goethite," Z. Kristallogr. **189**, 223–237.

Yang, S., Xu, Y., Sun, Y., Zhang, G., and Gao, D. (**2012**). "Size-controlled synthesis, magnetic property, and photocatalytic property of uniform α-Fe_2O_3 nanoparticles via a facile additive-free hydrothermal route," CrystEngComm **14**, 7915–7921.